# Elimination of Plasmon Losses and Enhanced Light Extraction of Top-Emitting Organic Light-Emitting Devices Using a Reflective Subelectrode Grid

Yue Qu,[†] Caleb Coburn,[‡] Dejiu Fan,[†] and Stephen R. Forrest*[,†,‡,§]

[†]Department of Electrical Engineering and Computer Science, [‡]Department of Physics, and [§]Department of Materials Science and Engineering, University of Michigan, Ann Arbor, Michigan 48109, United States

ABSTRACT: We demonstrate high-efficiency light extraction for top-emitting organic light-emitting devices (OLEDs) comprising a transparent conductive oxide on the surface of a nondiffractive, reflecting metal-coated scattering grid located beneath the organic active region. The grid scatters light trapped in waveguide modes without changing the device electrical properties or causing significant plasmonic losses. This results in an increase in external quantum efficiency for green phosphorescent organic light-emitting devices from $20 \pm 1\%$ to $30 \pm 2\%$, for structures without and with the reflecting grid. Adding a low refractive index capping layer reduces the spectral angular dependence characteristic of top-emitting OLEDs. The improvement in light extraction by substrate modification allows for optimization of the optical design without necessitating changes in the design or structure of the OLEDs themselves.

KEYWORDS: top-emitting OLED, outcoupling, cold-weld bonding, transparent contact
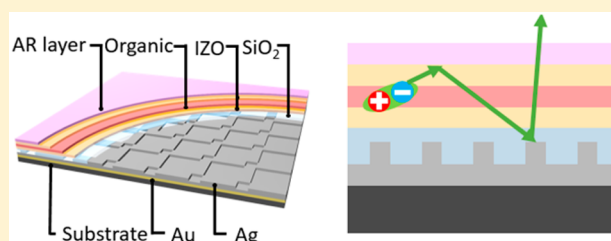
Organic light-emitting devices (OLEDs) are widely used for lighting and displays due to their many appealing characteristics such as high efficiency, wide color gamut, thin-film form factor, and flexibility.[1] Since phosphorescent OLEDs (PHOLEDs)[2,3] first realized a 100% internal quantum efficiency, light extraction has been the remaining bottleneck for improving power efficiency. Indeed, considerable work has been done to explain and overcome the low light extraction efficiency of conventional devices.[4−18] The major loss channels for trapped light (beyond modes trapped in the substrate) are waveguide and surface plasmon polariton (SPP) modes. Waveguide modes propagate tens of micrometers and can be efficiently scattered out of the device with appropriate outcoupling structures. In contrast, SSP modes are excited primarily in the metal cathode, propagate only a few micrometers, and dissipate before scattering.[7] Thus, suppressing SSPs while extracting waveguided power is a necessary strategy for achieving OLED external quantum efficiencies, η_{EQE}, greater than 70%.

Unlike bottom-emitting OLEDs, top-emitting devices emit through a semitransparent electrode into air and do not suffer from optical power trapping within the substrate. However, the higher reflectivity of the semitransparent top electrode creates a strong optical cavity that introduces additional lossy waveguide modes along with undesirable angle and wavelength dependences of the emission spectrum.[19] Furthermore, since both electrodes in top-emitting devices are often composed of metal, it is not possible to entirely suppress SPP modes using thick organic layers without also lowering efficiency.[10] Numerous methods have been proposed to overcome inefficient optical extraction in top-emitting devices that rely on three different mechanisms: cavity effects,[11,13,20] scattering light with corrugations,[14,21] and using microlens arrays (MLA) or scattering films on the device emitting surfaces.[10,12,15] However, enhancements of most of these strategies remain limited by the excitation of SPP modes.

Here we demonstrate an outcoupling scheme for top-emitting diodes by replacing both anode and cathode with indium zinc oxide (IZO)/ molybdenum trioxide (MoO$_3$) transparent contacts and placing a reflective and scattering corrugated metal-coated dielectric mirror beneath the electrically active organic region. This is combined with a low refractive index antireflection (AR) layer to reduce microcavity effects.

A schematic diagram of the device is shown in Figure 1. The design spaces the active region away from the metal reflector to minimize coupling to SPP modes while scattering out the waveguided optical power without disturbing the planarity of the device itself. Employing a scattering structure within the substrate while retaining a planar substrate surface allows complete freedom for optimizing the scattering layer dimensions without affecting the electrical properties of the OLED. The Ag reflector is a patterned grid of raised rectangles whose periodicity is on the order of several wavelengths to avoid angle- and wavelength-dependent effects. A dielectric spacer fills in the depressions and extends above the rectangular grid, providing a planar surface for the subsequent deposition of the electrodes and organic layers. The thick and thin spacer regions couple differently to the microcavity modes by locally
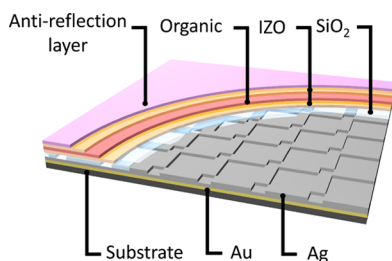
Figure 1. Schematic cut away view of top-emitting organic light emitting devices with indium zinc oxide (IZO)/MoO$_3$ electrodes and a metal-coated subelectrode grid. The low refractive index antireflection layer reduces microcavity effects. The Au layer bonds the subelectrode grid to the substrate.

creating both thick and thin cavity regions beneath the electrode.

To optimize the light extraction from the two cavities, the effects of the spacer thickness are determined using Green's function analysis,[22,23] as shown in Figure 2a. The active region used in simulating this structure comprises a 130-nm-thick organic layer (n_{org} = 1.8) sandwiched between 80-nm-thick transparent electrodes (50 nm IZO and 30 nm MoO$_3$, n_{IZO} = n_{MoO3} = 2), with the emission layer (EML) placed 60 nm above the bottom electrode. A randomly oriented green-emitting molecular dipole is placed at the position of the EML. The spacer refractive index is n = 1.5. The optical outcoupling efficiency is >20% when spacer layer thicknesses are 65 and 245 nm. Most of the optical power is lost into waveguide modes due to the elimination of SPPs, as shown in Figure 2a.

We investigate SPP coupling in the thick and thin cavities by calculating the local electric field of the plasmon mode at the EML, $\mathbf{E}(z)$. The emission rate into the SPP mode is found using Fermi's golden rule:

$$\Gamma(\omega) = \frac{2\pi}{\hbar} |\langle i|d \cdot \mathbf{E}(z)|f\rangle|^2 \rho(\hbar\omega) \tag{1}$$

where d denotes the exciton dipole moment, i and f the initial and final exciton state wave functions, and $\rho(\hbar\omega)$ the plasmonic mode density. The distance of the exciton from the metal interface is z, and $\mathbf{E}(z)$ is the electrical field of the SPP mode normalized to a half-quantum for zero-point fluctuations.[24] The magnetic field intensity profiles of SPP modes in the OLED cavities are shown in Figure 2b and c, found using the dispersion relation

$$k_{SPP}^2 = \frac{\varepsilon_m \varepsilon_d}{\varepsilon_m + \varepsilon_d}\left(\frac{2\pi}{\lambda}\right)^2 \tag{2}$$

where wavelength λ = 510 nm. Since the skin depths of the modes are comparable or even smaller than the dielectric thickness, we assume a semi-infinite metal layer having a dielectric constant ε_m[25] in contact with a semi-infinite dielectric layer with dielectric constant ε_d.

Figure 2b shows the calculated mode profiles in the regions where the cavity is thin (corresponding to the areas where the grid lines are raised) for different values of the index of refraction of the spacer layer, n. The calculated propagation lengths of SPP modes ($\delta_{SPP} = 1/[2\mathrm{Im}(k_{SPP})]$) are also shown. Both the field intensity in the EML whose position is denoted by the black dotted line and the propagation length decrease as the refractive index of the spacer layer increases. For comparison, the red dotted line indicates the distance from
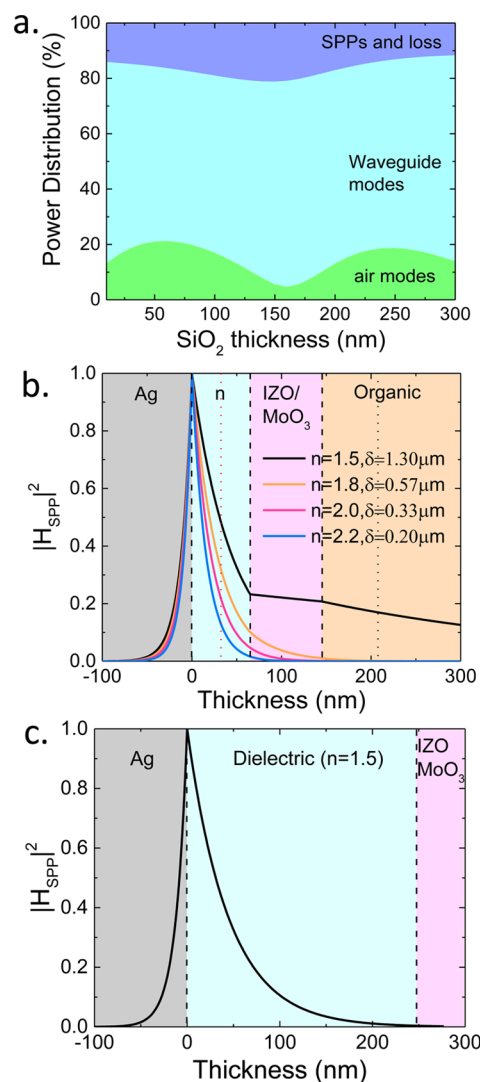

Figure 2. (a) Modal power distribution vs spacer layer thickness. The refractive index of the spacer is 1.5. (b) Surface plasmon mode magnetic field intensity across the control device structure with different refractive indexes, n. Also shown is the surface plasmon polariton (SPP) mode propagation length, δ. The structure is Ag/65 nm dielectric with variable n/60 nm IZO and MoO$_3$/organic layers (grid line area of the metal-coated grid). Emission layer position is denoted by the red dotted line. (c) Field intensity over deeper grid region, with dielectric layer thickness of 245 nm and n = 1.5 (depression area of the metal-coated grid).

the EML to the metal in a conventional top-emitting OLED (TEOLED). In that case, the local field of the SPP mode in the EML is larger than in our design (black dotted line), leading to a faster exciton coupling rate to SPPs. In Figure 2c, we observe that the SPP decays before reaching the organic layers in a thick cavity with n = 1.5. The coupling to SPP modes decays exponentially as the distance increases between the EML and metal surface. Thus, SPP coupling can be avoided with nonmetallic electrodes and the appropriate choice of spacer material and thickness.

The simulated modal power distributions of the cavities using Green's function analysis[22,23] are shown in Figure 3a and b. We define u as the ratio of the in-plane component of the wavevector, $k_{\parallel}$, for light propagating in the organic layers with a refractive index of n_{org}, to the total wavevector k, i.e., $u = k_{\parallel}/k$.
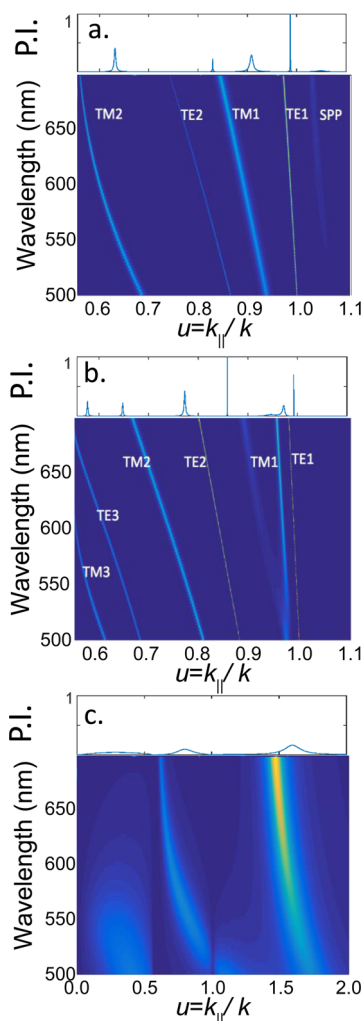
Figure 3. Modal power distributions within the cavities. Here, u is the in-plane component of the wavevector, $k_\parallel$, for light propagating within the organic layers with a refractive index of n_{org}, normalized to the wavevector k itself. The waveguide modes, and SPP modes at $u > n_{air}/n_{org}$, of the cavities over the (a) grid lines and (b) depression. (c) Power distribution of a conventional TEOLED optimized over the same spectral range, with the structure Ag/90 nm organic layers/20-nm-thick top Ag layer, with a 20 nm thick EML centered in the organic active region. The plots above each color map are the power distributions at a wavelength of $\lambda = 540$ nm.

Thus, the region at $u > 1$ corresponds to evanescent waves in the near field. Usually, modes with $u < n_{air}/n_{org}$ are radiative, those with $n_{air}/n_{org} < u < 1$ are waveguided, and modes in the region $u > 1$ are SPPs. For the thin cavity, there are four waveguide modes in the emission spectrum and a weak SPP mode. The thick cavity adds three more waveguide modes but has no SPP modes. Figure 3c shows the power distribution of a conventional TEOLED optimized over the same spectral range, with the structure Ag/90 nm organic layers/20-nm-thick top Ag layer, with a 20-nm-thick EML centered in the organic active region. This structure does not support waveguide modes, but has two SPP modes. The first SPP mode at $u \approx 0.6$ and $\lambda \approx 540$ nm is supported by the top thin Ag film. According to eq 2 and given $n_{air} < n_{org}$, this SPP mode lies in the region of $u < 1$ rather than $u > 1$ for organic/metal SSPs. The second SPP mode supported by the Ag/organic interface lies at $u > 1.5$. Figure 3a–c show that, compared to

conventional devices, both the control and metal-coated grid devices successfully suppress SPP modes while coupling more power into the waveguide modes.

The scattering by the grid is a consequence of the mismatch between the waveguide modes supported by the two cavities above the grid lines and depressions, which can be estimated by the overlap of the wavevectors of these modes. The TE1 and TM1 modes in the thin SiO$_2$ cavity (Figure 3a) have some overlap with the TE1 and TM1 modes in the thick cavity (Figure 3b), and thus these modes are inefficiently scattered. The modes that are not aligned between cavities are scattered by the grid. The spacer thicknesses determine the mismatch of the modes, but freedom to optimize the spacer thickness is limited when matching the cavity resonance to the OLED emission spectrum.

The simulated output of a dipole in the thin SiO$_2$ cavity regions using Green's function analysis,[22,23] shown in Figure 4a,
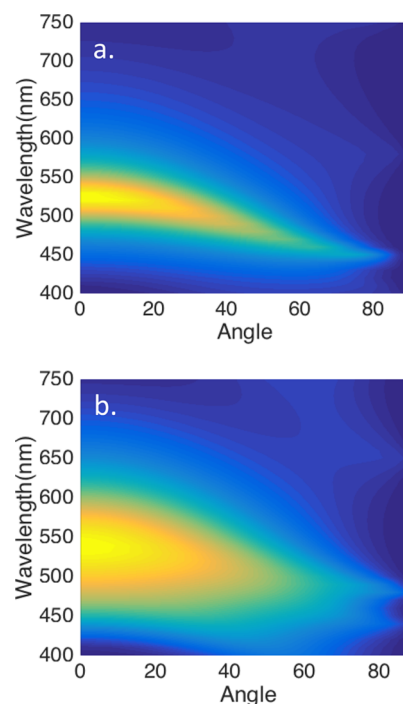

Figure 4. Simulated angle and wavelength dependence of the control device (a) without and (b) with a 70-nm-thick low-refractive ($n = 1.37$) antireflection (AR) coating. The device with the AR coating shows a broader spectrum and smaller blue shift at larger angles.

is strongly angle dependent. The spectral peak wavelength ranges from $\lambda = 545$ nm normal to the plane (0°) to $\lambda = 460$ nm at 90°. A 70-nm-thick low-refractive AR layer between air and the top IZO electrode reduces the cavity effects, as is apparent by the spread in wavelength emission and reduced blue shift with angle in Figure 4b. An example AR coating material is MgF$_2$, whose refractive index is $n_{MgF2} = 1.38$ in the range of the emission spectrum, close to the optimized value of $n = 1.4$ for IZO/air interfaces.

■ RESULTS

We fabricated an OLED using IZO/MoO$_3$ electrodes (control) and a device with a metal-coated grid having the same active layer, as follows starting from the substrate: 50 nm IZO/30 nm MoO$_3$/30 nm 4,7-diphenyl-1,10-phenanthroline (BPhen):Li
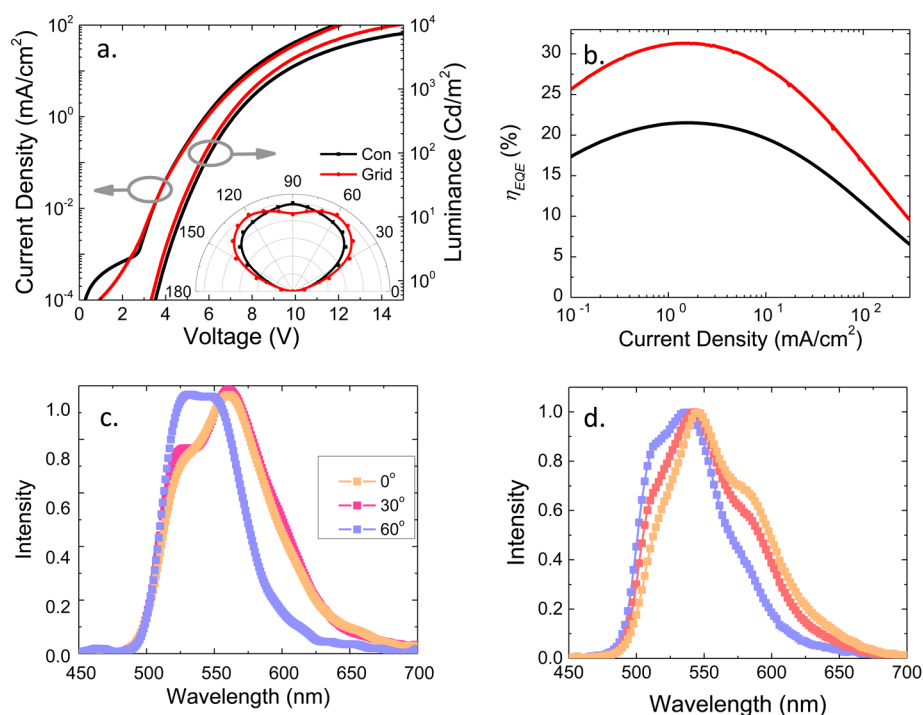
Figure 5. (a) Current density–voltage characteristics and (inset) the angular intensity profiles of the control (black) and metal-coated grid (red) devices. (b) External quantum efficiencies of the control and metal-coated grid devices. The emission spectra of the (c) control and (d) grid device with a MgF$_2$ AR coating at 0°, 30°, and 60° with 2° error.

(molar 1:1)/30 nm BPhen/30 nm Ir(ppy)$_3$ doped at 8 vol % in 4,4′-bis(carbazol-9-yl)biphenyl (CBP)/40 nm 4,4′-cyclohexylidenebis[N,N-bis(4-methylphenyl)benzenamine] (TAPC)/30 nm MoO$_3$/50 nm IZO. The bottom MoO$_3$ layer reduces electrical shorts that penetrate the spacer layer created by protrusions left from the grid lithography process.[26] The top MoO$_3$ layer prevents damage to the organic active region during the IZO sputtering process (see Methods). The control device has a 150 nm thick, planar Ag layer covered with a 65 nm SiO$_2$ spacer layer beneath the active region. The grid reflector is an array of 1×3 μm raised rectangles surrounding 3×3 μm and 1×1 μm square depressions, with the spacer thicknesses given above. Both devices are capped with a 70 nm thick MgF$_2$ AR coating. The current density–voltage curves of both devices are identical above turn on (~3 V), as shown in Figure 5a. Furthermore, η_{EQE} is increased from $20 \pm 1\%$ to $30 \pm 2\%$ using the metallic scattering grid, as shown in Figure 5b. The angular intensity profiles of the devices with the AR layer are broadened from a simple Lambertian emission profile. The peak intensity of the control device is normal to the surface, whereas the grid OLED intensity is at a maximum at 20° from normal. The spectra of the control (Figure 5c) and the metal-coated grid (Figure 5d) OLEDs are shown at 0°, 30°, and 60°. Both devices have spectral peaks at $\lambda \approx 550$ nm. Compared with the control, the grid device shows a slightly increased blue shift at large angles.

DISCUSSION

The emission intensity is a function of the overlap between the cavity resonance and the emission spectrum. The microcavity resonance peak (at $\lambda \approx 540$ nm, see Figure 4) is red-shifted from the emission spectral peak ($\lambda \approx 510$ nm). Thus, the blue shift with angle results in broader than the Lambertian angular intensity profiles for the control and grid devices shown in

Figure 4a, inset. The broadening of the grid OLED spectrum is more severe because the capping layer thickness, which reduces the cavity quality, was optimized for the thin cavity region of the grid devices, which is the same as the spacer layer thickness used in the control device.

Although a significant enhancement in efficiency is obtained using the reflecting grid, 60% of the optical power is still lost in the device. In addition to the limited grid scattering efficiency due to the spacer thickness used, the scattered light incurs losses at each reflection from the metal surface. A diffuser film or MLA comprised of high refractive index materials added to the top surface of the control devices should also generate higher efficiencies by reducing the cavity quality factor. The weaker cavity produced by these strategies is also beneficial for outcoupling white light. Using the fact that an MLA foil extracts more than half of the optical power going into the foil, the Green's function analysis shows that an MLA on the device emitting surface could further improve the efficiency by at least 30%.

CONCLUSIONS

In summary, a top-emitting device with IZO/MoO$_3$ electrodes has achieved $\eta_{EQE} = 20 \pm 1\%$, with almost no excitation of SPP modes. The efficiency is increased to $30 \pm 2\%$ by using a metal-coated scattering grid layer beneath the anode without impacting the OLED electrical characteristics. The efficiency can be further improved using an MLA or diffuser on the device emitting surface. The grid scatters the waveguided power and reduces plasmonic losses. The metallic scattering grid is fabricated within the substrate and hence, is totally separate from the organic active layers, allowing for considerable freedom in both the OLED and grid optical designs. Note that if the insulating spacer layer is replaced with a low-resistance transparent metal oxide, it can be used as a
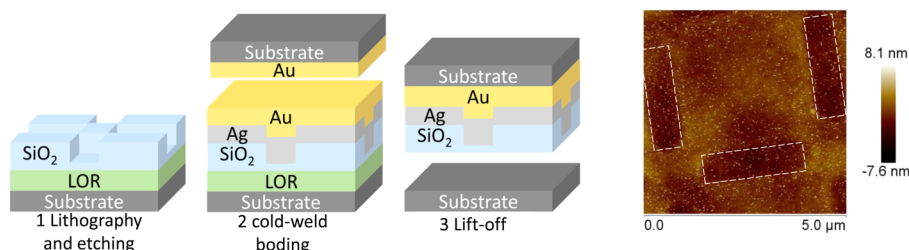
Figure 6. Fabrication sequence of the metal-coated grid and atomic force microscope image of the grid surface. There is deformation over the grid line area (indicated by dashed lines), and the root-mean-square surface roughness is 1.2 nm. The height difference due to the deformation is <5 nm.

conductive layer used for addressing OLED pixels in an active matrix display. This is just one of several possibilities allowed by this subelectrode light-scattering approach.

METHODS

The fabrication sequence for the metallic scattering layer is shown in Figure 6. A 245 nm SiO_2 film was deposited by electron-beam evaporation on a glass substrate precoated with sacrificial lift-off resist (MicroChem LOR 10B) (4000 rpm, 180 °C). Photoresist (Microposit S1813) was subsequently coated at 4000 rpm and cured at 115 °C for 90 s. The pattern was photolithographically defined using an AutoStep exposure system (GCA AS200) with an exposure time of 0.33 s. The 180 nm deep etch of the SiO_2 film was done using a 1:1 CF_4/CHF_3 plasma at 100 W. The photoresist was removed by exposure to oxygen plasma for 3 min at 800 W. Then a 150 nm thick Ag film was deposited by thermal evaporation after a 2-nm-thick Ti wetting layer. Next a 5-nm-thick Ge wetting layer followed by a 200-nm-thick Au film was deposited by electron-beam evaporation at 10 Å/s onto the surface of a clean glass and Ag/SiO_2/glass substrate. The two glass substrates were then sealed together via cold-weld bonding[27] by applying heat (200 °C) and pressure (4 MPa) for 5 min under vacuum (10^{-3} Torr) using an EVG 510 wafer bonder.[28] The bonding is sufficiently robust to survive sonication, although the Au surface on the grid is irregular due to the SiO_2 trenches, leaving vacancies at the bonding interface. The bonded glass slabs are diced into 1×1 in. squares, which were soaked in Remover PG (MicroChem at 80 °C) to dissolve the sacrificial LOR layer to leave the metallic-coated grid. After the grid preparation, a 50 nm thick IZO layer was deposited at 60 W in a chamber with an Ar pressure of 2 mTorr at a rate of 0.6 Å/s using a radio frequency magnetron sputterer.

The control substrate is prepared as follows: A glass substrate was cleaned using sonication in tergitol, deionized water, acetone, and isopropyl alcohol (IPA). A 2-nm-thick Ti wetting layer and 150-nm-thick Ag layer were sequentially deposited by thermal evaporation, followed by a 65-nm-thick SiO_2 film by electron-beam evaporation and 50-nm-thick IZO by sputtering (23 ohm/sq). The area was defined by a shadow mask without breaking vacuum between depositions.

The IZO-coated substrates were cleaned for 3 min by sonication in IPA and exposed to ultraviolet-ozone before PHOLED layer deposition by vacuum thermal evaporation in a system with a base pressure of 10^{-7} Torr. The first MoO_3 layer was deposited at 0.5 Å/s and the top MoO_3 layer at 0.05 Å/s for the first 5 nm and at 0.2 Å/s for the remaining thickness in the same chamber as the organic layers. The top IZO electrode was sputter-deposited in a chamber with an Ar pressure of 5 mTorr at 0.05 Å/s for the first 10 nm and 2 mTorr at 0.2 Å/s

for the remaining thickness. Finally, the MgF_2 capping layer was thermally deposited.

The refractive indexes and thicknesses of materials were measured using a variable-angle spectroscopic ellipsometer (J. A. Woollam WVASE32). Current−voltage−luminance characteristics were collected using a semiconductor parameter analyzer (HP-4156A) and a calibrated Si photodiode. The electroluminescence spectra were measured using an Ocean Optics miniature spectrometer. The η_{EQE} was calculated using standard methods.[29]

AUTHOR INFORMATION

Corresponding Author

*E-mail: stevefor@umich.edu.

ORCID

Stephen R. Forrest: 0000-0003-0131-1903

Notes

The authors declare the following competing financial interest(s): One of the authors (SRF) has a minor equity interest in a funder of this work (UDC).

ACKNOWLEDGMENTS

REFERENCES

(1) Forrest, S. R. The Path to Ubiquitous and Low-Cost Organic Electronic Appliances on Plastic. *Nature* 2004, 428, 911−918.

(2) Baldo, M. A.; O'Brien, D. F.; You, Y.; Shoustikov, A.; Sibley, S.; Thompson, M. E.; Forrest, S. R. Highly Efficient Phosphorescent Emission from Organic Electroluminescent Devices. *Nature* 1998, 395, 151−154.

(3) Adachi, C.; Baldo, M. A.; Thompson, M. E.; Forrest, S. R. Nearly 100% Internal Phosphorescence Efficiency in an Organic Light-Emitting Device. *J. Appl. Phys.* 2001, 90, 5048−5051.

(4) Koo, W. H.; Jeong, S. M.; Araoka, F.; Ishikawa, K.; Nishimura, S.; Toyooka, T.; Takezoe, H. Light Extraction from Organic Light-Emitting Diodes Enhanced by Spontaneously Formed Buckles. *Nat. Photonics* 2010, 4, 222−226.

(5) Sun, Y.; Forrest, S. R. Enhanced Light out-Coupling of Organic Light-Emitting Devices Using Embedded Low-Index Grids. *Nat. Photonics* 2008, 2, 483−487.

(6) Qu, Y.; Slootsky, M.; Forrest, S. R. Enhanced Light Extraction from Organic Light-Emitting Devices Using a Sub-Anode Grid. *Nat. Photonics* 2015, 9, 758−763.

(7) Chang, H.-W.; Lee, J.; Hofmann, S.; Hyun Kim, Y.; Müller-Meskamp, L.; Lüssem, B.; Wu, C.-C.; Leo, K.; Gather, M. C. Nano-Particle Based Scattering Layers for Optical Efficiency Enhancement of

Organic Light-Emitting Diodes and Organic Solar Cells. *J. Appl. Phys.* **2013**, *113*, 204502.

(8) Kim, J.-B.; Lee, J.-H.; Moon, C.-K.; Kim, S.-Y.; Kim, J.-J. Highly Enhanced Light Extraction from Surface Plasmonic Loss Minimized Organic Light-Emitting Diodes. *Adv. Mater.* **2013**, *25*, 3571−3577.

(9) Kim, S.-Y.; Jeong, W.-I.; Mayr, C.; Park, Y.-S.; Kim, K.-H.; Lee, J.-H.; Moon, C.-K.; Brütting, W.; Kim, J.-J. Organic Light-Emitting Diodes with 30% External Quantum Efficiency Based on a Horizontally Oriented Emitter. *Adv. Funct. Mater.* **2013**, *23*, 3896−3900.

(10) Hofmann, S.; Thomschke, M.; Freitag, P.; Furno, M.; Lüssem, B.; Leo, K. Top-Emitting Organic Light-Emitting Diodes: Influence of Cavity Design. *Appl. Phys. Lett.* **2010**, *97*, 253308.

(11) Schwab, T.; Schubert, S.; Hofmann, S.; Fröbel, M.; Fuchs, C.; Thomschke, M.; Müller-Meskamp, L.; Leo, K.; Gather, M. C. Highly Efficient Color Stable Inverted White Top-Emitting OLEDs with Ultra-Thin Wetting Layer Top Electrodes. *Adv. Opt. Mater.* **2013**, *1*, 707−713.

(12) Thomschke, M.; Reineke, S.; Lüssem, B.; Leo, K. Highly Efficient White Top-Emitting Organic Light-Emitting Diodes Comprising Laminated Microlens Films. *Nano Lett.* **2012**, *12*, 424−428.

(13) Fuchs, C.; Will, P.-A.; Wieczorek, M.; Gather, M. C.; Hofmann, S.; Reineke, S.; Leo, K.; Scholz, R. Enhanced Light Emission from Top-Emitting Organic Light-Emitting Diodes by Optimizing Surface Plasmon Polariton Losses. *Phys. Rev. B: Condens. Matter Mater. Phys.* **2015**, *92*, 245306.

(14) Schwab, T.; Fuchs, C.; Scholz, R.; Li, X.; Xie, F.; Choy, W.; Leo, K.; Gather, M. C. Improved Light Outcoupling and Mode Analysis of Top-Emitting OLEDs on Periodically Corrugated Substrates. *Proc. SPIE* **2013**, *8829*, 88291I.

(15) Yang, C.-J.; Liu, S.-H.; Hsieh, H.-H.; Liu, C.-C.; Cho, T.-Y.; Wu, C.-C. Microcavity Top-Emitting Organic Light-Emitting Devices Integrated with Microlens Arrays: Simultaneous Enhancement of Quantum Efficiency, cd/A Efficiency, Color Performances, and Image Resolution. *Appl. Phys. Lett.* **2007**, *91*, 253508.

(16) Koh, T.-W.; Spechler, J. A.; Lee, K. M.; Arnold, C. B.; Rand, B. P. Enhanced Outcoupling in Organic Light-Emitting Diodes via a High-Index Contrast Scattering Layer. *ACS Photonics* **2015**, *2*, 1366−1372.

(17) Brütting, W.; Frischeisen, J.; Schmidt, T. D.; Scholz, B. J.; Mayr, C. Device Efficiency of Organic Light-Emitting Diodes: Progress by Improved Light Outcoupling. *Phys. Status Solidi A* **2013**, *210*, 44−65.

(18) Lee, J.; Han, T.-H.; Park, M.-H.; Jung, D. Y.; Seo, J.; Seo, H.-K.; Cho, H.; Kim, E.; Chung, J.; Choi, S.-Y.; Kim, T.-S.; Lee, T.-W.; Yoo, S. Synergetic Electrode Architecture for Efficient Graphene-Based Flexible Organic Light-Emitting Diodes. *Nat. Commun.* **2016**, *7*, 11791.

(19) Gather, M. C.; Reineke, S. Recent Advances in Light Outcoupling from White Organic Light-Emitting Diodes. *J. Photonics Energy* **2015**, *5*, 57607.

(20) Schwab, T.; Schubert, S.; Müller-Meskamp, L.; Leo, K.; Gather, M. C. Eliminating Micro-Cavity Effects in White Top-Emitting OLEDs by Ultra-Thin Metallic Top Electrodes. *Adv. Opt. Mater.* **2013**, *1*, 921−925.

(21) Park, W.-Y.; Kwon, Y.; Lee, C.; Whang, K.-W. Light Outcoupling Enhancement from Top-Emitting Organic Light-Emitting Diodes Made on a Nano-Sized Stochastic Texture Surface. *Opt. Express* **2014**, *22*, A1687−A1694.

(22) Celebi, K.; Heidel, T.; Baldo, M. Simplified Calculation of Dipole Energy Transport in a Multilayer Stack Using Dyadic Green's Functions. *Opt. Express* **2007**, *15* (4), 327−334.

(23) Chance, R. R.; Prock, A.; Silbey, R. Lifetime of an Emitting Molecule near a Partially Reflecting Surface. *J. Chem. Phys.* **1974**, *60*, 2744.

(24) Gontijo, I.; Boroditsky, M.; Yablonovitch, E.; Keller, S.; Mishra, U. K.; DenBaars, S. P. Coupling of InGaN Quantum-Well Photo-luminescence to Silver Surface Plasmons. *Phys. Rev. B: Condens. Matter Mater. Phys.* **1999**, *60*, 11564−11567.

(25) Rakić, A. D.; Djurišić, A. B.; Elazar, J. M.; Majewski, M. L. Optical Properties of Metallic Films for Vertical-Cavity Optoelectronic Devices. *Appl. Opt.* **1998**, *37*, 5271−5283.

(26) Tyan, Y.-S.; Farruggia, G.; Cushman, T. R. P-173: Reduction of Shorting Defects in OLED Devices. *Dig. Tech. Pap. - Soc. Inf. Disp. Int. Symp.* **2007**, *38*, 845−848.

(27) Lee, K.; Shiu, K.-T.; Zimmerman, J. D.; Renshaw, C. K.; Forrest, S. R. Multiple Growths of Epitaxial Lift-off Solar Cells from a Single InP Substrate. *Appl. Phys. Lett.* **2010**, *97*, 101107.

(28) Fan, D.; Lee, K.; Forrest, S. R. Flexible Thin-Film InGaAs Photodiode Focal Plane Array. *ACS Photonics* **2016**, *3*, 670−676.

(29) Forrest, S. R.; Bradley, D. D. C.; Thompson, M. E. Measuring the Efficiency of Organic Light-Emitting Devices. *Adv. Mater.* **2003**, *15*, 1043−1048.